



Cite this: *Mater. Horiz.*, 2024, 11, 6150

Received 30th July 2024,  
Accepted 25th September 2024

DOI: 10.1039/d4mh00998c

rsc.li/materials-horizons

## Highly elastic relaxor ferroelectrics for wearable energy storage†

Liang Gao,<sup>a</sup> Jiaqi Zhang,<sup>bc</sup> Linping Wang,<sup>id</sup> \*<sup>a</sup> Dongyang Zhang,<sup>id</sup> <sup>a</sup> Fangzhou Li,<sup>a</sup> Haoyu Shen,<sup>a</sup> Ben-Lin Hu<sup>id</sup> \*<sup>a</sup> and Run-Wei Li<sup>id</sup> \*<sup>a</sup>

Polymer-based relaxor ferroelectrics with high dielectric constant are pivotal in cutting-edge electronic devices, power systems, and miniaturized pulsed electronics. The surge in flexible electronics technology has intensified the demand for elastic ferroelectric materials that exhibit excellent electrical properties and mechanical resilience, particularly for wearable devices and flexible displays. However, as an indispensable component, intrinsic elastomers featuring high dielectric constant and outstanding resilience specifically tailored for elastic energy storage remain undeveloped. Elastification of relaxor ferroelectric materials presents a promising strategy to obtain high-dielectric elastomers. In this study, we present a strain-insensitive, high elastic relaxor ferroelectric material prepared via peroxide crosslinking of a poly(vinylidene fluoride) (PVDF)-based copolymer at low temperature, which exhibits an intrinsic high dielectric constant ( $\sim 20$  at 100 Hz) alongside remarkable thermal, chemical, and mechanical stability. This relaxor ferroelectric elastomer maintains a stable energy density ( $> 8 \text{ J cm}^{-3}$ ) and energy storage efficiency ( $> 75\%$ ) under strains ranging from 0 to 80%. This strain-insensitive, high elastic relaxor ferroelectric elastomer holds significant potential for flexible electronic applications, offering superior performance in soft robotics, smart clothing, smart textiles, and electronic skin.

### New concepts

This paper presents a new concept of using peroxide cross-linking to prepare intrinsic high-elasticity relaxor ferroelectric materials for elastic energy storage. While relaxor ferroelectric materials for energy storage have been widely studied, current research primarily focuses on BTO-based composites, PMN-based materials, and PVDF-based terpolymers or quaterpolymers. These materials are typically brittle or plastic, failing to meet the elasticity demands of rapidly developing flexible electronics. Additionally, dielectric constant and breakdown field are crucial for energy storage materials. Some previous reports have attempted to achieve elasticity by blending elastomers with relaxor ferroelectrics, but this significantly increases the risk of electrical breakdown, making them unsuitable candidates. The newly developed elastic relaxor ferroelectric materials with high dielectric constants effectively address this issue, offering excellent elasticity and fatigue resistance. Our study provides a new approach to designing elastic energy storage materials, promising advancements in flexible electronics, and expanded applications in organic relaxor ferroelectric materials for elastic energy storage.

## Introduction

Electrostatic energy storage technology based on dielectric capacitors is renowned for its rapid charge-discharge rates and high power density, making it ideal for applications requiring energy delivery.<sup>1–4</sup> Therefore, dielectric capacitors are widely used as passive components for electrical energy storage and release in electronic devices, power systems, and electric vehicles.<sup>5,6</sup> Biaxially oriented polypropylene (BOPP) has garnered significant attention and usage in dielectric capacitors due to its high breakdown strength and extremely low dielectric loss (approximately 0.0002).<sup>7</sup> However, the highly symmetrical molecular structure of BOPP results in a low dielectric constant (2.2), limiting its discharge energy density to a modest  $2\text{--}4 \text{ J cm}^{-3}$  at  $25^\circ\text{C}$ .<sup>8</sup> This limited energy storage density restricts the application of BOPP in highly integrated, high-density miniaturized electronic devices, where enhanced energy storage capabilities are paramount.<sup>9</sup>

High dielectric-constant materials are primarily used in capacitors and other energy storage devices.<sup>10–13</sup> Among these, relaxor ferroelectric materials are emerging as highly promising

<sup>a</sup> CAS Key Laboratory of Magnetic Materials and Devices, and Zhejiang Province Key Laboratory of Magnetic Materials and Application Technology, Ningbo Institute of Materials Technology and Engineering, Chinese Academy of Sciences, 1219 West Zhongguan Road, Zhenhai District, Ningbo, P. R. China 315201.

E-mail: wanglinping@nimte.ac.cn, hubenlin@nimte.ac.cn, runweili@nimte.ac.cn

<sup>b</sup> Key Laboratory of Engineering Dielectrics and Its Application, Ministry of Education, Harbin University of Science and Technology, Harbin 150080, P. R. China

<sup>c</sup> School of Electrical and Electronic Engineering, Harbin University of Science and Technology, Harbin 150080, P. R. China

† Electronic supplementary information (ESI) available. See DOI: <https://doi.org/10.1039/d4mh00998c>

candidates for next-generation high-performance capacitors. This is due to their unique electrical properties, including high dielectric permittivity, broad temperature stability, and enhanced energy storage capability, which arise from their disordered nanoscale ferroelectric domains that rapidly respond to an electric field, generating polarization for efficient energy storage and release.<sup>14–17</sup> Energy storage in relaxor ferroelectric materials is achieved through polarization changes induced by an applied electric field. This process can be quantified using the formula

$$U_c = \int_{P_r}^{P_{\max}} E dP$$

where  $P_r$  and  $P_{\max}$  are the remanent and maximum polarization, respectively.  $P$  is the polarization,  $E$  is the applied electric field, and  $U_c$  denotes energy storage density.<sup>18</sup> Notable examples of such relaxor ferroelectric materials include barium titanate (BTO)-based composites and lead magnesium niobate (PMN)-based materials, which exhibit high dielectric constants and low losses, making them ideal for high-density energy storage.<sup>19,20</sup> For instance, samarium-doped bismuth ferrite-barium titanate (Sm-BFBT) exhibits superparamagnetic characteristics at high temperatures, significantly reducing hysteresis losses and enhancing its suitability for high-temperature applications.<sup>19</sup>

With the progression of flexible electronics technology, new requirements for the mechanical elasticity of materials have arisen.<sup>21–24</sup> In applications such as wearable devices, flexible displays, and bioelectronic devices, materials must not only exhibit excellent electrical properties but also withstand various deformations without compromising functionality. This has driven researchers to investigate elastic dielectric materials capable of meeting these stringent demands.<sup>25,26</sup> Our previous work introduced elasticity to relaxor ferroelectric materials through chemical crosslinking, successfully merging a high dielectric constant with exceptional mechanical elasticity. This innovation enables the material to maintain robust ferroelectric performance under complex deformation conditions, positioning elastic relaxor ferroelectric materials as strong contenders for dielectric energy storage applications.<sup>27,28</sup> However, challenges remain for elastic energy storage materials, including low energy storage density and variations in energy storage efficiency under strain. Consequently, the development of specifically designed for elastic energy storage has yet to be realized successfully.

To address this challenge, we focused on poly(vinylidene fluoride-chlorotrifluoroethylene) (P(VDF-CTFE)).<sup>29,30</sup> P(VDF-CTFE) is cost-effective and can be chemically modified in an alkaline environment to eliminate HCl forming P(VDF-CTFE-DB), which contains double bonds (DB) within the molecular chain.<sup>29</sup> This transformation of the bulky CTFE monomer into  $-C=C-$  bonds reduces spatial hindrance between molecular chains, facilitating the transition of P(VDF-CTFE-DB) from a paraelectric phase to a relaxor ferroelectric phase with enhanced ferroelectric characteristics. In previous work, crosslinking reactions typically required high temperatures,<sup>28,31,32</sup> posing a significant risk for CMOS or organic electronic processes.<sup>33–35</sup> Therefore, identifying a milder and more efficient crosslinking

method to achieve elasticity at lower temperatures was crucial. We strategically chose benzoyl peroxide (BPO) for crosslinking due to its lower initiation temperature ( $\sim 80^\circ\text{C}$ ) and high crosslinking efficiency.<sup>36,37</sup> The high reactivity of the  $-C=C-$  sites in the crosslinking material P(VDF-CTFE-DB) significantly reduces the crosslinking reaction temperature and enhances reaction efficiency. Additionally, triallyl isocyanurate (TAIC) was selected as a co-crosslinking agent to further boost crosslinking efficiency.<sup>38,39</sup>

In this work, we report an intrinsically elastic relaxor ferroelectric material prepared by peroxide crosslinking at a low crosslinking temperature ( $120^\circ\text{C}$ ). This material exhibits a dielectric constant of 19.4 at 100 Hz at room temperature, alongside exceptional elasticity and thermal, chemical, and mechanical stability. Moreover, it maintains an energy storage efficiency exceeding 75% at frequencies above 1000 Hz and under strain levels ranging from 0 to 80%, demonstrating stable storage capability under different strains ( $> 8\text{ J cm}^{-3}$  at  $300\text{ MV m}^{-1}$ ). Compared to the widely studied BOPP which has an energy density of  $2\text{--}4\text{ J cm}^{-3}$ , this new material showcases outstanding energy density and strain-insensitive energy storage characteristics. This advancement positions it as a highly promising candidate for next-generation energy storage applications in flexible and wearable electronics.

## Results and discussion

### Preparation of elastic relaxor ferroelectrics *via* peroxide crosslinking

The preparation of P(VDF-CTFE-DB) was carried out according to the previously reported method,<sup>29</sup> with its  $^1\text{H}$  NMR spectrum in acetone- $d_6$  presented in Fig. S1 (ESI<sup>†</sup>). P(VDF-CTFE-DB) was dissolved in acetone with a specific ratio of BPO and TAIC. The resulting solution was either cast or spin-coated onto substrates to form thick or thin films, respectively. After most of the acetone evaporated in a fume hood, the blended film was obtained by completely removing the solvent under vacuum at  $26^\circ\text{C}$ . Subsequent thermal crosslinking was conducted by heating the film on a heating stage in ambient air to obtain the crosslinked P(VDF-CTFE-DB).

The peroxide crosslinking mechanism is straightforward. During heating, the peroxide bonds in BPO undergo homolytic cleavage, yielding alkoxy free radicals.<sup>38</sup> These radicals subsequently attack the unsaturated  $C=C$  bonds within the PVDF (polyvinylidene fluoride)-based polymer, generating polymer free radical intermediates. These intermediates then interact with the allylic bonds present in the tri-functional TAIC (tri-allyl isocyanurate), initiating the crosslinking reaction.<sup>40,41</sup> This process forms a crosslinked network that enhances the thermal stability, mechanical properties, and chemical resistance of the polymer.

### Crosslinking and characterization of elastic relaxor ferroelectrics

Differential scanning calorimetry (DSC) analysis of the blended P(VDF-CTFE-DB) films illustrated in Fig. 1(A), revealed an

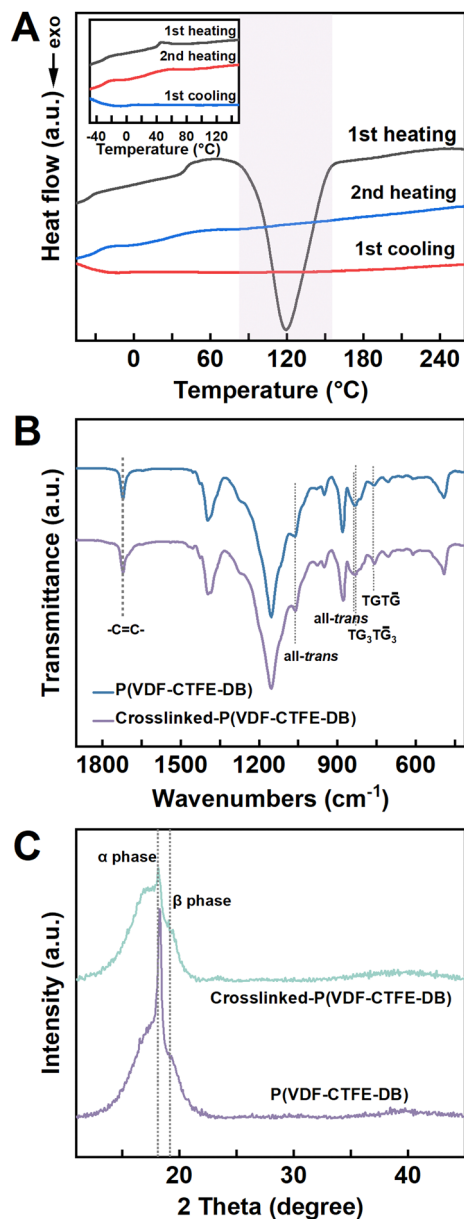


**Fig. 1** Crosslinking and crystalline properties of elastic relaxor ferroelectric films. (A) DSC curves of the blended P(VDF-CTFE-DB)/BPO/TAIC during heating and cooling cycles. (B) FT-IR spectra (C) and XRD patterns of pristine and crosslinked P(VDF-CTFE-DB).

exothermic peak corresponding to the crosslinking reaction within the temperature range of 80–160 °C, with a peak at 120 °C. Thermal treatment at 120 °C for one hour ensured complete crosslinking, as evidenced by the absence of an exothermic peak during the first heating cycle of the DSC curve for the crosslinked P(VDF-CTFE-DB) film (see inset of Fig. 1(A)). Consequently, this thermal treatment condition was employed for all subsequent experiments. Further DSC testing was conducted on crosslinked P(VDF-CTFE-DB) films with varying ratios of BPO and TAIC, as shown in Fig. S2(B) and (C) (ESI†). The results demonstrated that the content of the crosslinking initiator significantly impacted the melting temperature of the

crosslinked P(VDF-CTFE-DB) film. Specifically, an increase in the ratios of BPO and TAIC resulted in a consistent decrease in the crystalline melting enthalpy of the crosslinked P(VDF-CTFE-DB) film.

Crosslinked P(VDF-CTFE-DB) films exhibited notable resistance to common organic solvents such as cyclohexanone, acetone, dimethylformamide, and isophorone. After 15 days of immersion in these solvents, the crosslinked sample displayed swelling behavior with a gel content of approximately 90% (Fig. S3 and Table S1, ESI†).

Furthermore, in subsequent acid–base resistance tests, no significant volume changes were observed in the crosslinked P(VDF-CTFE-DB) films after two weeks of immersion in concentrated sulfuric acid and saturated sodium hydroxide aqueous solution, respectively (Fig. S4, ESI†). The crosslinked films also demonstrated excellent thermal stability, with a decomposition temperature ( $T_{d5\%}$ ) exceeding 367 °C, as evidenced by the thermogravimetric analysis curve (Fig. S5, ESI†).

Fourier-transform infrared spectroscopy (FT-IR) and X-ray diffraction (XRD) were employed to verify the crystalline structure in both pristine and crosslinked P(VDF-CTFE-DB) films, as depicted in Fig. 1(B) and (C). Notably, the C=C double bonds within the P(VDF-CTFE-DB) chain did not fully participate in the crosslinking process, as evidenced by the persistent presence of C=C double bonds at 1720  $\text{cm}^{-1}$  (Fig. 1(B)). The phase content analysis of P(VDF-CTFE-DB) before and after crosslinking was conducted with reference to previous studies.<sup>42,43</sup> The identification of existing phases was based on the appearance of specific characteristic bands (listed in Table S2, ESI†), followed by calculations using specific equations depending on whether the sample contained  $\alpha$ - and  $\beta$ -phases or  $\alpha$ - and  $\gamma$ -phases. Further details are provided in Supplementary Note (ESI†). After crosslinking, the content of the  $\alpha$ -phase (764  $\text{cm}^{-1}$ ) increased from 14.7% to 47.48%, and the  $\beta$ -phase (840  $\text{cm}^{-1}$ ) rose from nearly 0 to 52.52%. The X-ray diffraction (XRD) analysis (Fig. 1(C)) also clearly shows changes in the crystalline phases of the films before and after crosslinking. Although the crystallinity of the films decreased after crosslinking, leading to reduced diffraction peak intensity, the  $\beta$ -phase diffraction peak at 19.2° remains visible.

### Mechanical properties of elastic relaxor ferroelectrics

Stress–strain tests were conducted on crosslinked P(VDF-CTFE-DB) films with varying ratios of BPO and TAIC, as depicted in Fig. 2. For BPO ratios below 4%, the stress–strain curves exhibited a distinct yielding point, indicating that the pristine and lightly crosslinked P(VDF-TrFE-DB) still retained plastic deformation characteristics (Fig. 2(A) and Fig. S6, ESI†). In contrast, when the ratio of BPO exceeded 4%, no yielding point was observed. Notably, as the crosslinking density increased, the Young's modulus and elongation at break of the crosslinked samples decreased sharply (Fig. 2(B)). A comparison of the cyclic performance of samples with 12% and 18% BPO ratios, which exhibited similar Young's moduli, is shown in Fig. S7 (ESI†). It was found that the sample with 12% BPO displayed superior recovery performance under larger tensile cycles. Therefore, considering the desirable attributes

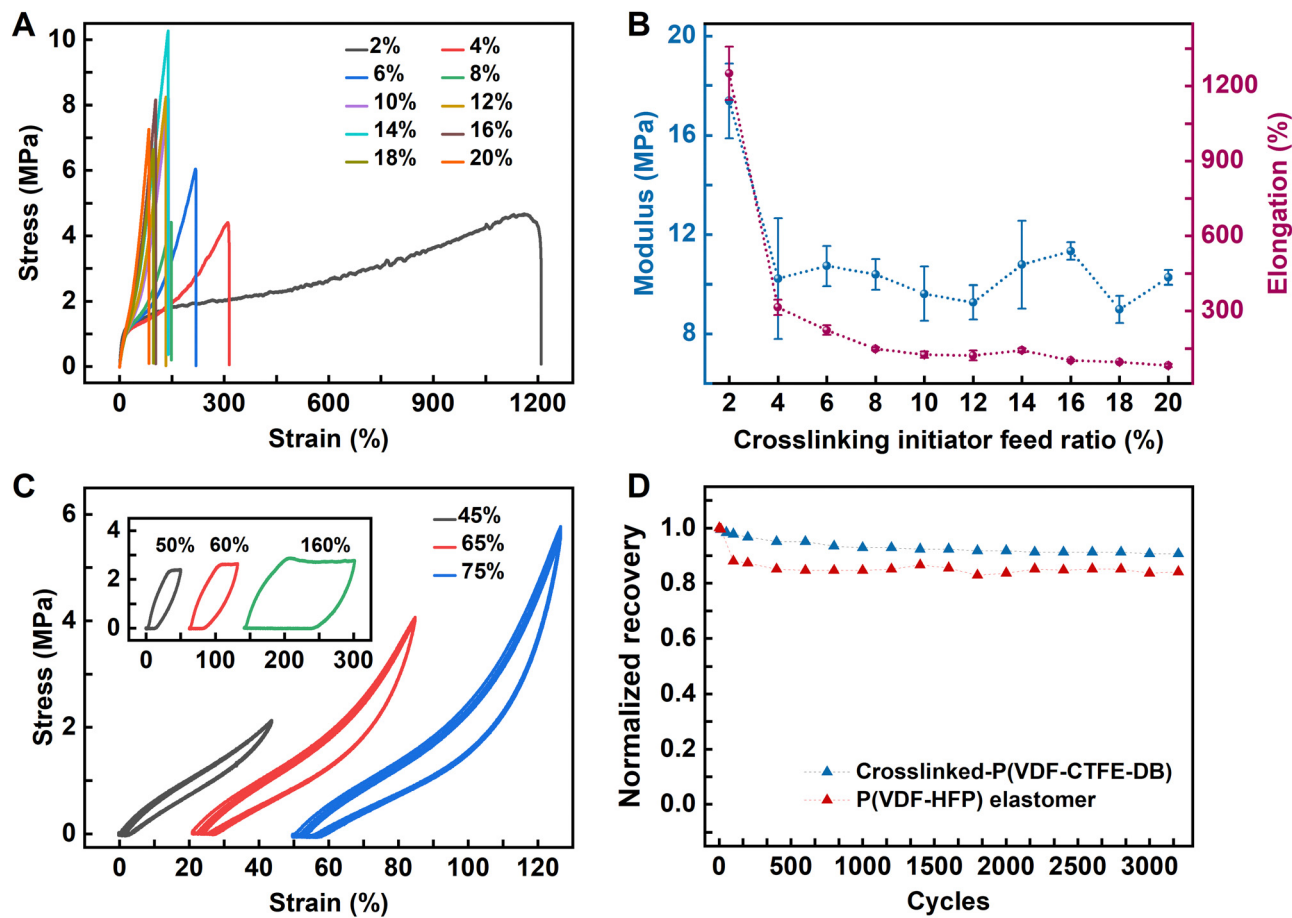


Fig. 2 Mechanical properties of elastic relaxor ferroelectrics films. (A) Stress–strain curves of crosslinked P(VDF-CTFE-DB) films at various BPO ratios. (B) Young's modulus and elongation at break of crosslinked P(VDF-CTFE-DB) films with different BPO ratios. (C) Cyclic stress–strain curves of crosslinked P(VDF-CTFE-DB) films with a BPO ratio of 12% and pristine P(VDF-CTFE-DB) films (inset) under different strains (the first cycle is omitted owing to clamp sliding and the X-axis is shifted for clarity). (D) Fatigue resistance of crosslinked P(VDF-CTFE-DB) film with a BPO ratio of 12% under 50% strain, compared to that of a commercial fluororubber P(VDF-HFP) (DAI-EL, G-801).

of low Young's modulus, high elastic recovery, and high crystallinity (Fig. S2D, ESI†) for elastic polymer ferroelectrics, the crosslinked P(VDF-CTFE-DB) with a BPO ratio of 12% was selected as the optimized sample for all subsequent experiments.

The elastic recovery of the crosslinked P(VDF-CTFE-DB) was evaluated through cyclic stress–strain measurements under strains ranging from 45 to 75% (5 cycles in Fig. 2(C) and over 3000 cycles under 50% strain as shown in Fig. 2(D)). Compared to the pristine P(VDF-CTFE-DB) samples (inset of Fig. 2(C)), the crosslinked films exhibited excellent elastic recovery. During the initial cycles, the recovery exceeded 95%, and after 600 cycles of stretching and releasing, the elastic recovery remained stable, exceeding 90% without significant decline. Compared to commercial fluororubber, the crosslinked P(VDF-CTFE-DB) film exhibited superior fatigue resistance and higher recovery ratios. The elasticity of crosslinked P(VDF-CTFE-DB) was attributed to entropy elasticity rather than energy elasticity, as estimated by the “force–temperature” curve of crosslinked P(VDF-CTFE-DB) under different strains (Fig. S8, ESI†). These results affirm that the intrinsic elasticity of polymer relaxor ferroelectrics can be obtained through peroxide crosslinking at a low temperature.

### Relaxor ferroelectricity of crosslinked P(VDF-CTFE-DB)

To confirm the relaxor ferroelectric behavior of the crosslinked P(VDF-TrFE-CTFE) film, we conducted comprehensive characterizations utilizing polarization–electric field ( $P$ – $E$ ) loops, temperature-dependent dielectric constant ( $\epsilon$ – $T$ ) curves, and piezoresponse force microscopy (PFM). The  $P$ – $E$  and  $\epsilon$ – $T$  tests were conducted using a capacitor configuration, transforming the capacitance into polarization or dielectric constants. The results are illustrated in Fig. 3.

A capacitor-type device was fabricated to measure the  $\epsilon$ – $T$  curves of both pristine and crosslinked P(VDF-CTFE-DB) films. The  $\epsilon$ – $T$  curves of crosslinked P(VDF-CTFE-DB) are shown in Fig. 3(A). Compared to the pristine P(VDF-CTFE-DB) (Fig. S9, ESI†), the crosslinked film exhibits a broader ferroelectric-to-paraelectric ( $F$ – $P$ ) transition temperature range and a higher dielectric constant of 19.4 at 100 mHz under room temperature. Additionally, the Curie temperature ( $T_c$ ) shifts to higher temperatures with increasing frequency, indicating the presence of relaxation behavior in the crosslinked P(VDF-CTFE-DB). The  $P$ – $E$  loops of crosslinked P(VDF-CTFE-DB) were obtained using a sandwich structure device (Au/crosslinked-P(VDF-CTFE-DB)/Au/Si). As



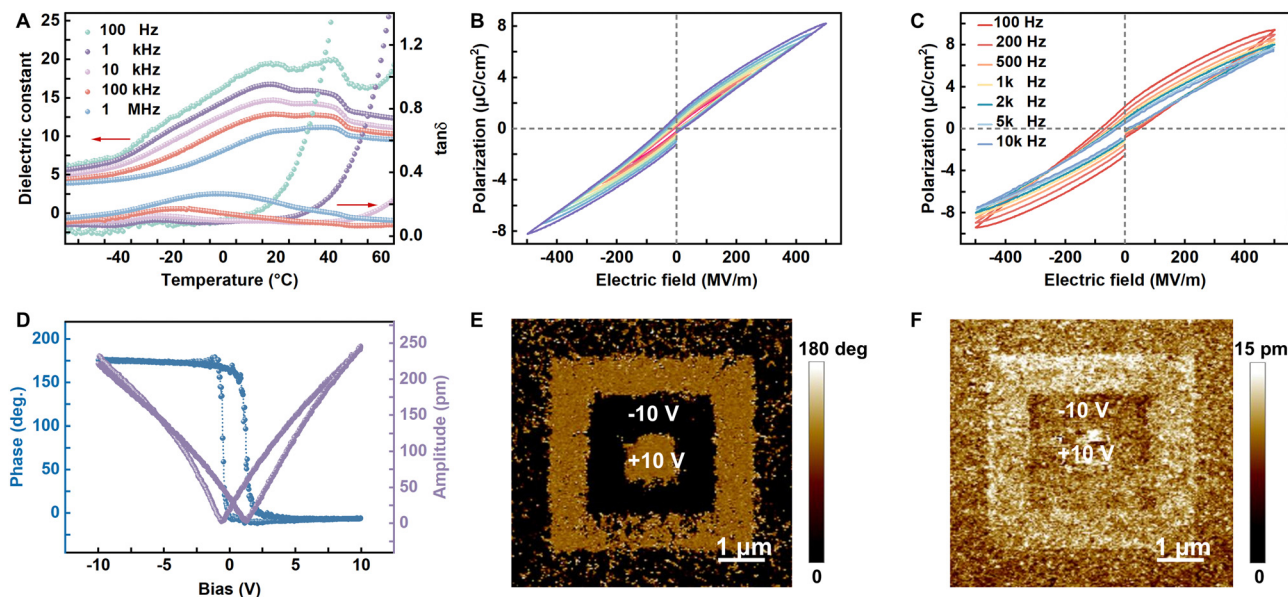


Fig. 3 Ferroelectric properties of crosslinked P(VDF-CTFE-DB) films. (A) Temperature-dependent  $\epsilon$  and dielectric loss of crosslinked P(VDF-TrFE-DB) films at different frequencies. (B), (C)  $P$ - $E$  loops of Au/C-P(VDF-CTFE-DB)/Au under varying electric fields at 1000 Hz (B) and at different frequencies (C). (D) Phase-voltage hysteresis and amplitude-voltage butterfly loop. (E), (F) Phase (E) and amplitude (F) mapping were obtained from PFM.

shown in Fig. 3(B), the loops exhibited low rectangularity, and appeared slender, which is a typical feature of a relaxor ferroelectric material. As the applied electric field increases, the initial hysteresis maintains its slender shape, characterized by a significantly large ratio between  $P_{\text{max}}$  and  $P_r$ , resulting in lower rectangularity. At 1 kHz and 500 MV  $\text{m}^{-1}$ , the  $P_{\text{max}}$  and  $P_r$  of the crosslinked P(VDF-CTFE-DB) film are 8.2 and 1.05  $\mu\text{C cm}^{-2}$ , respectively. In comparison, the pristine P(VDF-CTFE-DB) exhibits  $P_{\text{max}}$  and  $P_r$  values of 3.32 and 0.52  $\mu\text{C cm}^{-2}$  at 280 MV  $\text{m}^{-1}$  and 1 kHz, respectively (Fig. S10A, ESI†). The coercive field ( $E_c$ ) of crosslinked P(VDF-CTFE-DB) is approximately 47 MV  $\text{m}^{-1}$ . The  $P_r$  of the crosslinked P(VDF-CTFE-DB) increases from 0.46 to 2.13  $\mu\text{C cm}^{-2}$  across test frequencies ranging from 10 kHz to 100 Hz (Fig. 3(C)). Compared to pristine P(VDF-CTFE-DB) (Fig. S10B, ESI†), the crosslinked P(VDF-CTFE-DB) film exhibits more pronounced relaxor behavior due to the more condensed network introduced by peroxide crosslinking, which further breaks down the crystalline domains.

PFM was used to evaluate the piezoelectric properties of the crosslinked P(VDF-CTFE-DB) films. This technique enabled the visualization of local polarization domains and provided quantitative data on the piezoelectric coefficients. The crosslinked P(VDF-CTFE-DB) films exhibited enhanced piezoelectric responses compared to the pristine samples (Fig. S11, ESI†), confirming the improved ferroelectric relaxor behavior (Fig. 3(D)-(F)). The hysteresis and butterfly curves obtained from a single scan demonstrate the complete switching of ferroelectric domains under the influence of an electric field (Fig. 3(D)).

By applying a +10 V bias to a  $5 \times 5 \mu\text{m}^2$  region, followed by a -10 V bias to a  $3 \times 3 \mu\text{m}^2$  region, and finally a +10 V bias to a  $1 \times 1 \mu\text{m}^2$  region, phase and amplitude maps of a “box in box” pattern were obtained (Fig. 3(E) and (F)). This pattern suggests that the polarity of the ferroelectric domains in the

crystalline structure can be reversibly switched by an applied field in a defined area rather than just at a single point. Additionally, PFM revealed a piezoelectric coefficient of 11.57 pm  $\text{V}^{-1}$  (Fig. S12, ESI†), indicating well piezoelectric performance. Relaxor ferroelectricity response and energy storage characteristics of crosslinked P(VDF-CTFE-DB) under strain.

To evaluate the relaxor ferroelectric response and energy storage properties of crosslinked-P(VDF-CTFE-DB) films under strain, we fabricated a fully elastic capacitive ferroelectric device as shown in Fig. 4(A). Flexible interdigitated electrodes were prepared using liquid metal gallium mixed with gallium oxide, with PDMS serving as the elastic substrate, and crosslinked P(VDF-CTFE-DB) films acting as the intermediate dielectric layer. The elastic device was affixed in a custom-made single-shaft tensile clamp and gradually stretched to 80% strain, as depicted in Fig. 4(B). The test results are summarized in Fig. 4(C)-(H). The  $P$ - $E$  loops of this fully elastic device (Fig. S13, ESI† and Fig. 4(C)) without strain are comparable to those of the rigid device with Au electrodes. Additionally, without strain, as the frequency increases (from 100 Hz to 10 kHz), the  $P_{\text{max}}$  and  $P_r$  of the crosslinked film slightly decrease. The energy storage density and efficiency were calculated at different frequencies, showing that the energy storage efficiency increases from 32.9% at 100 Hz to 90.7% at 10 kHz, while the energy storage density shows a minor decline, from 7.6 to 6.0 J  $\text{cm}^{-3}$  at 300 MV  $\text{m}^{-1}$ . These results indicate good energy storage density and efficiency at frequencies of 1000 Hz and above (Fig. 4(D) and (E)).

The  $P_{\text{max}}$  and  $P_r$  remain almost constant throughout the stretching process (Fig. 4(F), (G) and Fig. S14-S21, ESI†), which forms the basis for its strain insensitivity as an energy storage material. The energy storage density and efficiency were calculated under different strains (0–80%) at 330 MV  $\text{m}^{-1}$ , and the

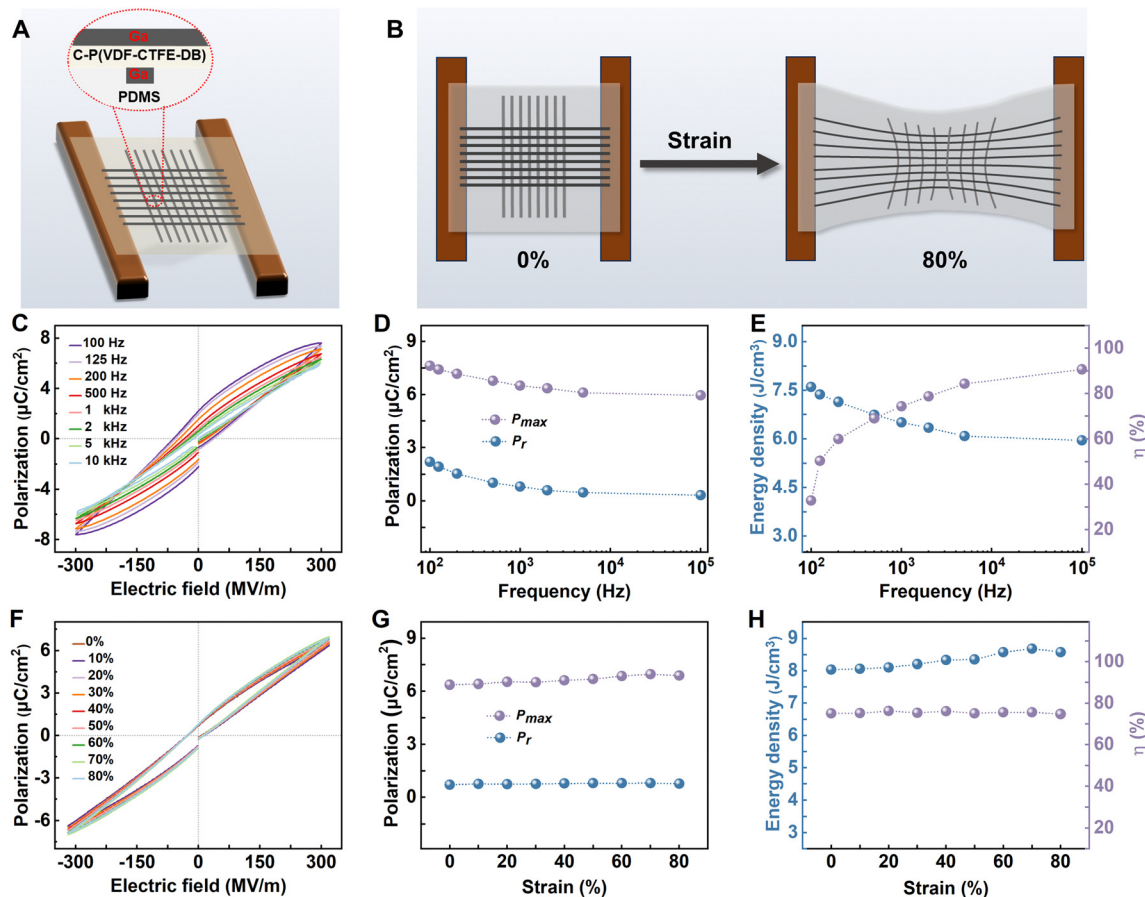


Fig. 4 FE response of elastic relaxor ferroelectrics under strains. (A), (B) Schematic structure of elastic device (A) and its setup under 0 and 80% strain (B). (C)  $P$ - $E$  loops at 0% strain across frequencies ranging from 100 Hz to 10 kHz. (D, E) Variation of  $P_r$ ,  $P_{max}$  (D) and energy density,  $\eta$  (E) under different frequencies. (F)  $P$ - $E$  loops at 1 kHz under strain ranging from 0 to 80%. (G, H) Changes in  $P_r$ ,  $P_{max}$  (G) and energy density,  $\eta$  (H) under different strains.

energy storage efficiency remained above 75%, maintaining a high energy storage density ( $>8.0 \text{ J cm}^{-3}$ ) (Fig. 4(H)). Traditional PVDF and its copolymers usually exhibit changes in crystal structure under tensile strain.<sup>44,45</sup> However, due to the stress dispersion provided by the crosslinked network, the crystalline structure remains stable during stretching, resulting in consistent electrical performance.

To ensure the reliability of energy storage, we conducted electrical breakdown tests on the films before and after cross-linking. Aluminum electrodes with a diameter of 3 mm were deposited on the surface of the 10  $\mu\text{m}$  thick films, and DC voltage was used for the electrical breakdown tests, as shown in Fig. S22 (ESI<sup>†</sup>). The breakdown strength of the crosslinked films significantly improved, with the pristine P(VDF-CTFE-DB) film exhibiting a breakdown field of  $202 \text{ MV m}^{-1}$  at a 63.2% breakdown probability, and the crosslinked P(VDF-CTFE-DB) film showing an increased breakdown field of  $255 \text{ MV m}^{-1}$ .

Compared to the breakdown field observed during  $P$ - $E$  loop testing, the electric breakdown tests on the 10  $\mu\text{m}$  thick films likely include more film defects and consider factors such as the edge effects of the electric field due to the larger electrode size, which generally results in a lower measured breakdown

field. Consequently, we calculated the energy storage density and efficiency under different strains at a test field of  $230 \text{ MV m}^{-1}$  (Fig. S23, ESI<sup>†</sup>). The energy storage efficiency consistently remained above 80%, with energy storage density always exceeding  $4.5 \text{ J cm}^{-3}$ . This demonstrates the reliability of our testing and calculation of energy storage efficiency and density are reliable when miniaturizing the device.

#### Relaxor ferroelectricity response and energy storage characteristics of crosslinked P(VDF-CTFE-DB) under strain

Elastic relaxor ferroelectric elastomers, with high dielectric constant, low modulus, and strain-insensitive energy storage properties, could potentially be highly suitable for applications in the field of elastic electronics. These materials could revolutionize soft robotics by providing flexible, lightweight, and efficient power sources that facilitate versatile movements and operations without compromising flexibility. Integrating strain-insensitive elastic dielectric energy storage materials into soft robots could ensure that they possess the necessary energy to operate effectively. Looking ahead, smart clothing and textiles stand to benefit significantly from these materials. Embedding elastic dielectric energy storage materials into fabrics could power embedded sensors, heating elements, and electronic

devices, enabling wearable health monitoring, environmental sensing, and self-heating functionalities. Additionally, next-generation display technologies, such as flexible and rollable OLED displays, could utilize these materials to maintain a continuous power supply during bending and unfolding. This advancement would ensure that displays remain functional and reliable, even under significant physical deformation.

## Conclusions

We successfully developed a highly elastic relaxor ferroelectric material using peroxide crosslinking reactions, which maintains a stable ferroelectric response under strains of up to 80%. The crosslinked P(VDF-CTFE-DB) features a relatively high dielectric constant ( $\sim 20$  at 100 Hz) and a low modulus ( $< 10$  MPa), along with superior fatigue resistance compared to commercial fluorooelastomers, as well as excellent thermal and chemical stability. Due to its remarkable strain-insensitive ferroelectric response, high dielectric constant, and high elasticity, it maintains an energy density above  $8 \text{ J cm}^{-3}$  and an energy storage efficiency of over 75% under strains up to 80%. These results position the elastic relaxor ferroelectric as a promising candidate for elastic energy storage applications. Our strategy offers a novel approach to the elastification of relaxor ferroelectric materials, providing a new high-dielectric elastomer for applications in flexible electronics, such as soft robotics, smart clothing, smart textiles, and electronic skin.

## Experimental section

A detailed Experimental section can be found in the ESI.†

## Author contributions

BLH and LG conceived this study. LG wrote the draft, BLH and LPW revised the manuscript. LG, LPW and BLH designed the experiments, analysed the results. BLH and RWL supervised this study. All authors have given approval to the final version of the manuscript.

## Data availability

The data supporting this article have been included as part of the ESI.†

## Conflicts of interest

The authors declare that they have no known competing financial interests or personal relationships that could have appeared to influence the work reported in this paper.

## Acknowledgements

This work was supported by Zhejiang Provincial Natural Science Foundation of China (LR24E030003), Zhejiang Province

Qianjiang Talent Program (ZJ-QJRC-2020-32), National Natural Science Foundation of China (51931011, 52127803), and “Pioneer” and “Leading Goose” R&D Program of Zhejiang (2022C01032).

## References

- 1 Z. M. Dang, J. K. Yuan, S. H. Yao and R. J. Liao, *Adv. Mater.*, 2013, **25**, 6334–6365.
- 2 B. J. Chu, X. Zhou, K. L. Ren, B. Neese, M. R. Lin, Q. Wang, F. Bauer and Q. M. Zhang, *Science*, 2006, **313**, 334–336.
- 3 Q. Li, L. Chen, M. R. Gadinski, S. H. Zhang, G. Z. Zhang, H. U. Li, E. Iagodkine, A. Haque, L. Q. Chen, T. N. Jackson and Q. Wang, *Nature*, 2016, **536**, 112.
- 4 H. Palneedi, M. Peddigari, G. Hwang, D. Jeong and J. Ryu, *Adv. Funct. Mater.*, 2018, **28**, 1803665.
- 5 Q. Wang and L. Zhu, *J. Polym. Sci., Part B: Polym. Phys.*, 2011, **49**, 1421–1429.
- 6 Q. Li, F. Z. Yao, Y. Liu, G. Z. Zhang, H. Wang and Q. Wang, *Annu. Rev. Mater. Res.*, 2018, **48**, 219–243.
- 7 H. Janet and T. R. Jow, *IEEE Trans. Dielectr. Electr. Insul.*, 2012, **19**, 990–995.
- 8 X. Yuan, Y. Matsuyama and T. C. M. Chung, *Macromolecules*, 2010, **43**, 4011–4015.
- 9 C. Chen, L. Shen, G. Liu, Y. Cui and S. Yan, *Polymers*, 2024, **16**, 1058.
- 10 P. Khanchaitit, K. Han, M. R. Gadinski, Q. Li and Q. Wang, *Nat. Commun.*, 2013, **4**, 2845.
- 11 C. Wu, X. Huang, X. Wu, L. Xie, K. Yang and P. Jiang, *Nanoscale*, 2013, **5**, 3847–3855.
- 12 A. Ling, A. B. Steven and P. C. Jeffrey, *IEEE Electr. Insul. Mag.*, 2008, **24**, 5–10.
- 13 H. Pan, S. Lan, S. Xu, Q. Zhang, H. Yao, Y. Liu, F. Meng, E. Guo, L. Gu, D. Yi, R. X. Wang, H. Huang, J. L. MacManus-Driscoll, L. Chen, K. Jin, C. Nan and Y. Lin, *Science*, 2021, **374**, 100–104.
- 14 B. Yang, Q. Zhang, H. Huang, H. Pan, W. Zhu, F. Meng, S. Lan, Y. Liu, B. Wei, Y. Liu, L. Yang, L. Chen, C. Nan and Y. Lin, *Nat. Energy*, 2023, **8**, 956–964.
- 15 P. Zhao, H. Wang, L. Wu, L. Chen, Z. Cai, L. Li and X. Wang, *Adv. Energy Mater.*, 2019, **9**, 1803048.
- 16 L. Wu, X. Wang and L. Li, *RSC Adv.*, 2016, **6**, 14273–14282.
- 17 Z. Shen, X. Wang, B. Luo and L. Li, *J. Mater. Chem. A*, 2015, **3**, 18146–18153.
- 18 L. Yang, X. Kong, F. Li, H. Hao, Z. Cheng, H. Liu, J. Li and S. Zhang, *Prog. Mater. Sci.*, 2019, **102**, 72–108.
- 19 H. Pan, F. Li, Y. Liu, Q. Zhang, M. Wang, S. Lan, Y. Zheng, J. Ma, L. Gu, Y. Shen, P. Yu, S. Zhang, L. Chen, Y. Lin and C. Nan, *Science*, 2019, **365**, 578–582.
- 20 J. Kim, S. Saremi, M. Acharya, G. Velarde, E. Parsonnet, P. Donahue, A. Qualls, D. Garcia and L. W. Martin, *Science*, 2020, **369**, 81–84.
- 21 T. Someya, Z. Bao and G. G. Malliaras, *Nature*, 2016, **540**, 379–385.
- 22 J. Xu, S. Wang, G.-N. Wang, C. Zhu, S. Luo, L. Jin, X. Gu, S. Chen, V.-R. Feig, J. W. F. To, S. Rondeau-Gagné, J. Park,

- B. C. Schroeder, C. Lu, J. Y. Oh, Y. Wang, Y. Kim, H. Yan, R. Sinclair, D. Zhou, G. Xue, B. Murmann, C. Linder, W. Cai, J. B. H. Tok, J. W. Chung and Z. Bao, *Science*, 2017, **355**, 59–64.
- 23 Y. Jiang, Z. Zhang, Y. Wang, D. Li, C. Coen, E. Hwaun, G. Chen, H. Wu, D. Zhong, S. Niu, W. Wang, A. Saberi, J. Lai, Y. Wu, Y. Wang, A. A. Trotsyuk, K. Y. Loh, C. Shih, W. Xu, K. Liang, K. Zhang, Y. Bai, G. Gurusankar, W. Hu, W. Jia, Z. Cheng, R.-H. Dauskardt, G. C. Gurtner, J. B. H. Tok, K. Deisseroth, I. Soltesz and Z. Bao, *Science*, 2022, **375**, 1411–1417.
- 24 Y. Zheng, Y. Liu, D. Zhong, S. Nikzad, S. Liu, Z. Yu, D. Liu, H. Wu, C. Zhu, J. Li, H. Tran, J. B. H. Tok and Z. Bao, *Science*, 2021, **373**, 88–94.
- 25 D. Jung, C. Lim, H. J. Shim, Y. Kim, C. Park, J. Jung, S.-I. Han, S. Sunwoo, K. W. Cho, G. D. Cha, D. C. Kim, J. H. Koo, J. H. Kim, T. Hyeon and D. Kim, *Science*, 2021, **373**, 1022–1026.
- 26 J. A. Rogers, T. Someya and Y. Huang, *Science*, 2010, **327**, 1603–1607.
- 27 B. W. Li, L. P. Wang, L. Gao, T. H. Xu, D. Y. Zhang, F. Z. Li, J. Lyu, R. Zhu, X. Gao, H. Zhang, B. L. Hu and R. W. Li, *Angew. Chem., Int. Ed.*, 2024, **63**, e202400511.
- 28 T. H. Xu, L. P. Wang, L. Gao, F. Z. Li, B. Hu, B. W. Li, H. Y. Shen, Z. Liu and B. L. Hu, *Adv. Mater.*, 2024, e2404001.
- 29 S. B. Tan, J. J. Li, G. X. Gao, H. Y. Li and Z. C. Zhang, *J. Mater. Chem.*, 2012, **22**, 18496–18504.
- 30 S. B. Tan, X. Hu, S. J. Ding, Z. C. Zhang, H. Y. Li and L. J. Yang, *J. Mater. Chem. A*, 2013, **1**, 10353–10361.
- 31 L. Gao, B. L. Hu, L. P. Wang, J. W. Cao, R. He, F. Y. Zhang, Z. M. Wang, W. H. Xue, H. L. Yang and R. W. Li, *Science*, 2023, **381**, 540–544.
- 32 L. P. Wang, L. Gao, B. W. Li, B. Hu, T. H. Xu, H. Lin, R. Zhu, B. L. Hu and R. W. Li, *J. Am. Chem. Soc.*, 2024, **146**, 5614–5621.
- 33 A. Kyaw, F. Jamalullah, L. Vaithieswari, M. J. Tan, L. Zhang and J. Zhang, *ACS Appl. Mater. Interfaces*, 2016, **8**, 9533–9539.
- 34 H. J. Kim, A. R. Han, C. H. Cho, H. Kang, H. H. Cho, M. Y. Lee, J. Frechet, J. H. Oh and B. J. Kim, *Chem. Mater.*, 2012, **24**, 215–221.
- 35 J. I. Park, J. W. Chung, J. Y. Kim, J. Lee, J. Y. Jung, B. Koo, B. L. Lee, S. W. Lee, Y. W. Jin and S. Y. Lee, *J. Am. Chem. Soc.*, 2015, **137**, 12175–12178.
- 36 C. Han, X. Ran, X. Su, K. Zhang, N. Liu and L. Dong, *Polym. Int.*, 2007, **56**, 593–600.
- 37 J. W. Huang, Y. J. Jin, X. L. Han, Y. Wu, H. F. Tian, S. Men and J. Hu, *Polym. Bull.*, 2024, **81**, 6905–6920.
- 38 J. B. Finlay, A. Hallenbeck and J.-D. MacLachlan, Peroxide-Curable Fluoroelastomers, *J. Elastomers Plast.*, 1978, **10**, 3–16.
- 39 G. Kojima and H. Wachi, Vulcanization of a fluoroelastomer derived from tetrafluoroethylene and propylene, *Rubber Chem. Technol.*, 1978, **51**, 940–947.
- 40 W. Naebpetch, B. Junhasavasdikul, A. Saetung, T. Tulyapitak and N. Nithi-Uthai, *Plast., Rubber Compos.*, 2016, **45**, 436–444.
- 41 J. Y. Wang, S. S. Pan, Y. Zhang and S. R. Guo, *Polym. Test.*, 2017, **59**, 253–261.
- 42 N. Meng, X. T. Ren, G. Santagiuliana, L. Ventura, H. Zhang, J. Wu, H. Yan, M. J. Reece and E. Bilotti, *Nat. Commun.*, 2019, **10**, 4535.
- 43 X. M. Cai, T. P. Lei, D. H. Sun and L. W. Lin, *RSC Adv.*, 2017, **7**, 15382.
- 44 R. Guo, H. Luo, X. F. Zhou, Z. D. Xiao, H. R. Xie, Y. Liu, K. C. Zhou, Z. H. Shen, L. Q. Chen and D. Zhang, *J. Mater. Chem. A*, 2021, **9**, 27660–27671.
- 45 R. Guo, H. Luo, D. Zhai, Z. D. Xiao, H. R. Xie, Y. Liu, F. Wang, X. Jiang and D. Zhang, *Adv. Powder Mater.*, 2024, **3**, 100212.